Opto-Electronic Advances

CN 51-1781/TN ISSN (Print) 2096-4579 ISSN (Online) 2097-3993

Triplet exciton harvesting via TADF in hafnium chlorides array scintillator screen enables ultrahigh-resolution X-ray imaging

Jun'an Lai, Yi Ye, Xu Liu, Sijun Cao, Shiji Zhou, Wenxia Zhang, Kang An, Peng He, Tingming Jiang, Xiaosheng Tang*, Rui Zhou* and Dong Zhang*

Citation: Lai JA, Ye Y, Liu X et al. Triplet exciton harvesting via TADF in hafnium chlorides array scintillator screen enables ultrahigh-resolution X-ray imaging. *Opto-Electron Adv* **9**, 250273 (2026).

https://doi.org/10.29026/oea.2026.250273

Received: 11 October 2025; Accepted: 11 February 2026; Published online: 16 April 2026

OEA | Opto-Electronic Advances

Article

June 2026, Vol. 9, No. 6

Open Access

Triplet exciton harvesting via TADF in hafnium chlorides array scintillator screen enables ultrahigh-resolution X-ray imaging

Jun'an Lai[1,2†], Yi Ye[3†], Xu Liu[1], Sijun Cao[2], Shiji Zhou[2], Wenxia Zhang[4], Kang An[2], Peng He[2], Tingming Jiang[2], Xiaosheng Tang[2,4*], Rui Zhou[5,6*] and Dong Zhang[1*]

Abstract: Indirect X-ray imaging is an indispensable non-destructive testing technology in the medical and industrial fields. However, its quality is restricted by the light output and optical crosstalk of the scintillation screens. Herein, we report a series of hafnium-based organic-inorganic metal halides (OIMHs) with regulated organic cation chain lengths. The thermally activated delayed fluorescence (TADF) is demonstrated in these materials by their anti-thermal quenching luminescence characteristics, fitting of temperature-dependent photoluminescence decay lifetime, and a series of theoretical calculations. These represent non-luminescent triplet excitons that can be emitted by reverse intersystem crossing (RISC), thus improving the utilization rate of excitons and increasing the light output of scintillators. The highest performance of our reported hafnium-based OIMHS shows a light yield of 56563.31±1250 photons/MeV and detection limit of 23.86 nGy_{air}/s. Moreover, the optical crosstalk is suppressed by developing silicon array scintillation screens, and an ultra-high spatial resolution of 31.41 lp/mm is achieved. These results offer insights into the luminescent mechanism of hafnium-based OIMHs and initiate a new paradigm for exciton-optical co-management for high-quality X-ray imaging.

Keywords: X-ray imaging; metal halide scintillator; thermally activated delayed fluorescence; light management

DOI: 10.29026/oea.2026.250273 | CSTR: 32247.14.oea.2026.250273

Citation: Lai JA, Ye Y, Liu X et al. Triplet exciton harvesting via TADF in hafnium chlorides array scintillator screen enables ultrahigh-resolution X-ray imaging. *Opto-Electron Adv* **9**, 250273 (2026).

1 Introduction

X-ray imaging plays an indispensable role in medical diagnosis, industrial inspection, and security[1–4], due to its ability to reveal internal structures through differential X-ray attenuation[5]. The X-ray detection modalities include direct and indirect[6,7]. The indirect detection dominates owing to its mature technology and excellent compatibility with silicon sensors[8]. The performance of scintillators is a key factor affecting indirect X-ray detection[9]. Traditional scintillation screens built by Gd_2O_2S:Tb (GOS) are cheap and flexible yet suffers from strong light scattering and low resolution (~6.3 lp/mm)[10], while CsI:Tl scintillation screens achieve higher resolution (~10 lp/mm) but show poor stability, toxicity, and high cost[11]. Thus, new scintillators with high atomic numbers, strong radioluminescence, and stability are urgently needed[12,13]. Metal halide perovskites like $CsPbX_3$(X=Cl, Br, I)[14], with low cost, tunable band gaps, and solution processability, are promising[15]. However, $CsPbX_3$ suffers from toxicity and self-absorption. Recent advances in low-dimensional halides enhance radioluminescence via quantum confinement, with hafnium-based OIMHs emerging as strong candidates due to their high atomic number and light yield[16].

Received: 11 October 2025

Accepted: 11 February 2026

Published online: 16 April 2026

[1]Department of Radiology, Xinqiao Hospital, Army Medical University, Chongqing 400037, China; [2]Key Laboratory of Optoelectronic Technology & Systems (Ministry of Education), College of Optoelectronic Engineering, Chongqing University, Chongqing 400044, China; [3]Emergency Department of the Affiliated Hospital/College of Clinical Medicine, Guizhou Medical University, Guiyang 550000, China; [4]College of Optoelectronic Engineering, Chongqing University of Posts and Telecommunications, Chongqing 400065, China; [5]Institute of Optics and Electronics, Chinese Academy of Sciences, Chengdu 610209, China; [6]Pen-Tung Sah Institute of Micro-Nano Science and Technology, Xiamen University, Xiamen 361005, China.

†These authors contributed equally to this work.

*Correspondence: XS Tang, E-mail: xstang@cqu.edu.cn; R Zhou, E-mail: zhour@ioe.ac.cn;
D Zhang, E-mail: hszhangd@tmmu.edu.cn

The Cs_2HfCl_6 (CHC) was reported with a high atomic number (Z=72) and a light yield of 54000 photons/MeV, comparable to NaI(Tl), which attracted great attention[17]. However, the reported light yields vary significantly with preparation methods, and the luminescence mechanism of CHC remains controversial[18]. Different studies attribute its emission to charge transfer in $[HfCl_6]^{2-}$ clusters[17], trapped excitons[19], self-trapped excitons[20], or Cl-related hole self-capture[21]. In addition, due to the similarity in chemical and physical properties between Zr and Hf elements, Zr ions may also affect the luminescence of CHC[22]. The presence of Zr may have side effects on the performance of CHC[23]. CHC belongs to the A_2BX_6 family (A represents +1 valence cations such as K, Rb, Cs, B represents +4 valence cations such as W, Mo, Zr, and Hf, and X represents halogen ions)[24], where isolated $[BX_6]^{2-}$ octahedra form zero-dimensional clusters with strong ligand-to-metal charge transfer (LMCT)[25], resembling complexes and organic molecules. Similar compounds, such as Cs_2ZrCl_6, have exhibited thermally activated delayed fluorescence (TADF)[26]. In such d^0 metal halides, LMCT states readily achieve efficient emission, and TADF properties are strongly affected by ligand field strength, conjugation, geometry, and environment through modulation of singlet–triplet energy gaps[27].

In this work, a series of hafnium-based OIMHs namely TTAHC (TTA_2HfCl_6), TECHC (TEA_2HfCl_6), TMAHC (TMA_2HfCl_6), TPAHC (TPA_2HfCl_6), and TBAHC (TBA_2HfCl_6) were developed. The crystal structure of the Hf-based OIMHs can be regulated by the carbon chain length of the organic cations. As the carbon chain length increased, the bond angle between the Hf-Cl band and the $[HfCl_6]^{2-}$ octahedral clusters became distorted. As the change of $[HfCl_6]^{2-}$ octahedral clusters, the charge transfer process from Cl^- ions to Hf^{4+} ions became regulated, and TADF emission was realized by reverse intersystem crossing (RISC). Ultimately, a light yield of up to 56563.31 photons/MeV was achieved for TMAHC. The pixel array structure is a key strategy for improving the resolution of detectors[28,29]. Herein, the light crosstalk was suppressed by developing an array scintillation screen to regulate the luminescence of the scintillators, and a spatial resolution of up to 33.14 lp/mm was achieved. Our work systematically studied exciton regulation and light management in scintillators, proposed a TADF luminescence mechanism for hafnium-based OIMHs scintillators, and developed a scintillation screen for high-resolution imaging, providing a paradigm for subsequent research on scintillation screens.

2 Result and discussion

2.1 The phase structure and properties

High-purity Hf raw materials were employed to mitigate the impact of Zr on the analysis of the luminescence mechanism. As detailed in the Supplementary information, all the samples were synthesized using a slow-cooling solvothermal method. The crystal structures of the prepared hafnium-based OIMHs are shown in Fig. 1(a) and Fig. S1. With an increase in the carbon chain length, the spacing between the $[HfCl_6]^{2-}$ octahedral clusters and the degree of distortion of the $[HfCl_6]^{2-}$ octahedral clusters increased. As the detail crystal parameters of hafnium-based OIMHs shown in shown in Table S1, the single crystal X-ray diffraction (SC-XRD) results reveal that the TTAHC, TEAHC, TMAHC, TPAHC and TBAHC crystallizes in the Fd-3c, C12/c1, P121/n1, P121/n1, and P121/n1 space group, with CCDC number of 2339395, 2221622, 2221623, 2339167 and 2339168. All hafnium-based OIMHs were built using organic cations and $[HfCl_6]^{2-}$ octahedral clusters. In the $[HfCl_6]^{2-}$ octahedral clusters, the Hf-Cl is opposite the central atom, and the organic cations consist of an N-central atom bonded to four different alkylamines. As depicted in Fig. 1(b), the hafnium-based OIMHs exhibit a white transparent crystal appearance in daylight and emit blue light under 254 nm illumination. Figure 1(c) and Fig. S2(a–e) show the powder X-ray diffraction (PXRD) patterns of the hafnium-based OIMHs. The experimental PXRD patterns perfectly matched with the CHC standard PDF card No. 032-0233, all the PXRD patterns of the prepared hafnium-based OIMHs matched with the fitted ones, indicating the pure phase of the prepared samples.

The stability of scintillators is related to their long-term performance characteristics. Figure S2(f) displays the phase stability of TMAHC tested using XRD. The XRD patterns of the samples aged for 1, 6, and 12 months were consistent with those of the fresh samples, without the generation of new substances. Figure S2(g) shows the thermodynamic stability of TMAHC tested by thermogravimetric analysis/differential scanning calorimetry (TGA/DSC) using a simultaneous thermal analyzer, which indicates that TMAHC retains its crystal structure after calcination at 400 °C in air. Figure S2(h) shows the humidity stability of the TTAHC, TMAHC, and TPAHC samples, which indicates that hafnium-based OIMHs with long carbon chains are less hygroscopic. This may be due to the ability of larger organic cations to shield the $[HfCl_6]^{2-}$ octahedral clusters from the influence of water molecules.

The X-ray photoelectron spectroscopy (XPS) was employed to characterize the elements and valence states of the hafnium-based OIMHs. The total XPS spectra of the elements in TTAHC, TEAHC, TMAHC, TPAHC, and TBAHC are shown in Fig. S3(a, d, g, j), and S3(m), respectively, proving the existence of N, Hf, and Cl in all the samples. Figure S3(b, e, h, k), and S3(n) show the XPS spectra of Hf in the above samples, with binding energies of Hf of approximately 18 and 20 eV, which match the $4f_{3/2}$ and $4f_{5/2}$ orbit of Hf^{4+} ions[19]. Figure S3(c, f, i, l) and S3(o) show the XPS spectra of Cl in the above samples, with the binding energies of hafnium at approximately 198 and 200 eV, which match the $2p_{3/2}$ and $2p_{5/2}$ orbit of Cl^- ions[30]. All XPS results

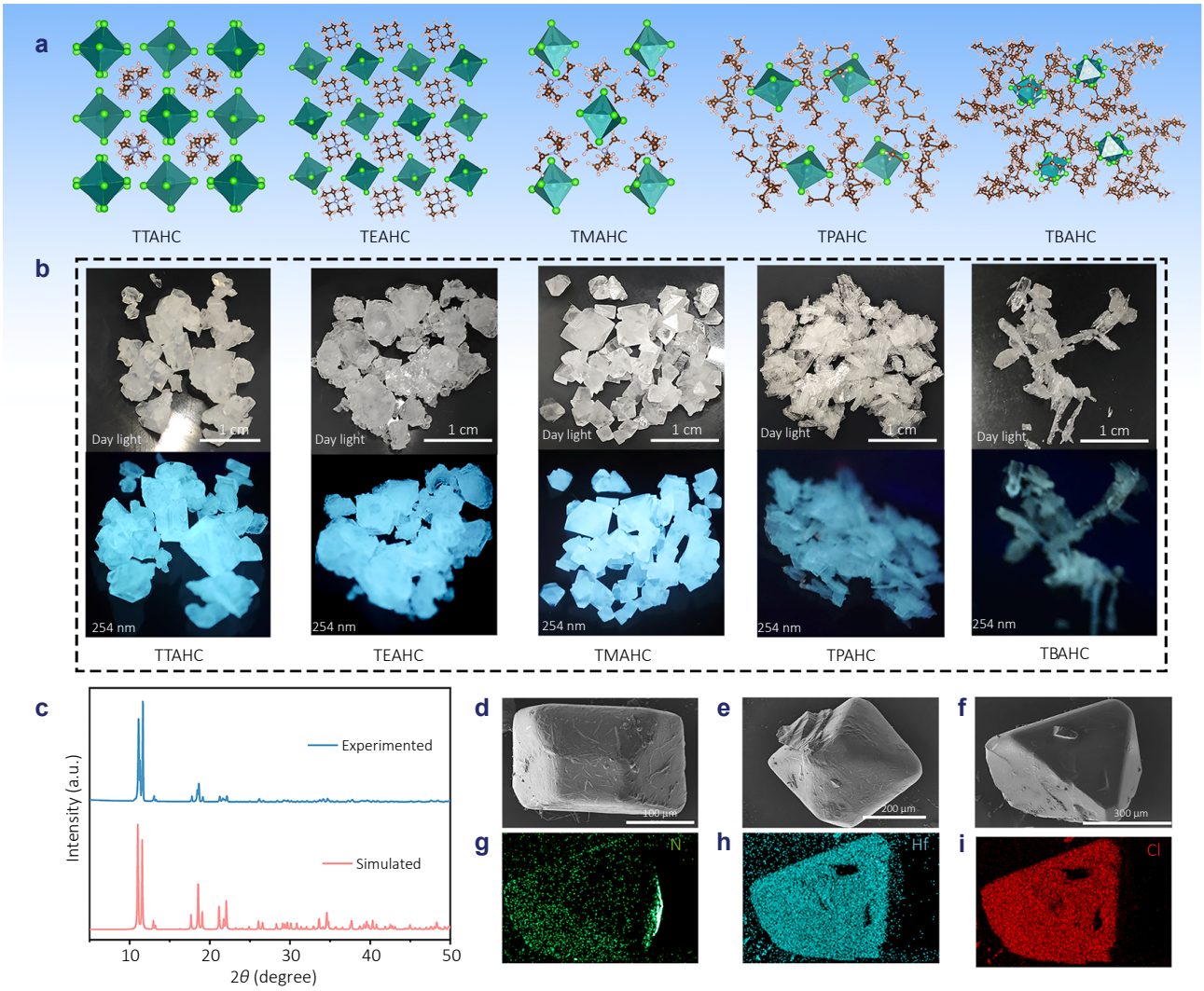

Fig. 1 | (a) The crystal and phase structure of prepared hafnium-based OIMHs. (b) The digital photograph under day light and 254 nm light. (c) The PXRD patterns of TMAHC. (d–f) SEM images of TMAHC. (g–i) Element distribution of EDS testing of TMAHC.

indicate that the hafnium and chlorine elements exist in the form of Hf^{4+} and Cl^- ions, respectively.

As the Zr content has a significant impact on the analysis of Hf-based metal halides, the elemental contents were analyzed using inductively coupled plasma-mass spectrometry (ICP-MS). The elemental distribution of TMAHC is shown in Table S2, where the contents of Hf and Zr are 26.18% and 0.01%, respectively, indicating almost no zirconium in the TMAHC. In addition, there were no emissive ns^2 ions for interfering luminescence analysis. The microstructure of the TMAHC crystals was explored using scanning electron microscopy (SEM), as shown in Fig. 1(d–f). The selected TMAHC crystals had smooth, regular octahedral structures. Figure 1(g–i) show the element distribution of the TMAHC crystal in Fig. 1(f) tested using an energy-dispersive spectrometer (EDS), which indicates a uniform distribution of Hf, nitrogen, and Cl elements.

2.2 The photoluminescence characteratics

The photoluminescence performance of the prepared Hf-based OIMHs were investigated. First, ultraviolet-visible (UV-Vis) absorption spectra were obtained, as shown in Fig. S4(a–f). All hafnium-based OIMHs showed similar absorption spectra, with the absorption coefficient increasing sharply at wavelengths below 400 nm and showing strong absorption in the deep shortwave ultraviolet region. The hafnium-based OIMHs exhibited two distinct absorption peaks. Previous reports attributed the absorption peak around 240–300 nm to sub-bandgap defects[19], while the peak around 320 nm was caused by the instrument changing the lamp. The optical bandgaps of TTAHC, TEAHC, TMAHC, TPAHC, and TBAHC were fitted using the Tauc plot[31], with values of 4.93, 4.82, 4.80, 4.62, and 4.79 eV, respectively, as shown in the insets of Fig. S4(a–e). Interestingly, all hafnium-based OIMHs exhibited excitation-

wavelength-dependent emission. As shown in the digital photograph of TMAHC in Fig. S4(f), the TMAHC crystal exhibits different emission colors that vary with the excitation wavelength. To investigate these characteristics, the excitation-wavelength-dependent emission spectra of the hafnium-based OIMHs were tested, as shown in Fig. S5. All samples exhibited similar luminescence performance, with sharp emission peaks at approximately 388 nm under excitation at 200 nm, and broadband emission peaks under longer excitation wavelengths. Typically, Fig. S5(c) and S5(d) show the excited wavelength-dependent emission of TMAHC in different wavelength ranges, indicating four emission models: the 350–400 nm range emission under 200–210 nm excitation, the 350–550 nm emission under 230–250 nm excitation, the 300–360 nm emission under 260–280 nm excitation, and the 600–750 nm emission under 280–380 nm excitation. The typical $[ZrCl_6]^{2-}$ impurity luminescence in CHC samples was 434 nm[32], which was not observed in the samples synthesized TMAHC. The photoluminescence (PL) spectra of the hafnium-based OIMHs excited at 240 nm are shown in Fig. S6(a), which is consistent with the trend in Fig. 1(b), indicating the best PL performance of TMAHC. As shown in Fig. S6 (b), after being stored for 12 months, the PL intensity tested under the same conditions decreased by 12.8%, which demonstrated excellent PL stability of TMAHC. The normalized PL intensity of TMAHC at different excitation wavelengths is shown in Fig. S6(c), which further indicates the excitation-dependent PL emission of TMAHC. The typical PL and photoluminescence excitation (PLe) spectra of TMAHC are presented in Fig. S6 (d), which reveals that TMAHC shows a narrow band emission peak at 388 nm under 200 nm excitation, and the PLe peaks correspond to the absorption spectrum. As shown in Fig. S6(e) and S6(f), the photoluminescence quantum yield (PLQY) excited by 254 nm and 270 nm are 42.8% and 11.5%. Owing to the high error of the PLQY test excited by deep ultraviolet band using existing instruments, the PLQY under 200 nm excitation cannot be calculated.

To comprehend the excitation wavelength-dependent PL emission of the hafnium-based OIMHs, the PL decay lifetimes were measured monitored at the four emission peaks, as illustrated in Fig. S7. The PL decay lifetime for the TAMHC emission at 388 nm, when excited at 200 nm, is 4.25 μs. The emission at 330 nm has a decay lifetime of approximately 1.2 μs, the emission at 460 nm is 1.3 μs, and the emission at 570 nm is about 1.8 μs. These differences in the PL decay lifetimes enabled the separation of the four emission centers. Additionally, a series of temperature-dependent PL characteristics were conducted to investigate the mechanism of the hafnium-based OIMHs. As shown in Fig. 2(a), the temperature-dependent Ple spectra by monitoring the 460 nm emission show abnormal anti-thermal quenching, which is consistent with the behavior of the charge transfer state[33]. As shown in Fig. 2(d), the temperature-dependent spectra of TMAHC excited at 200 nm also show anti-thermal quenching, which possibly originates from TADF. The temperature-dependent PL performance of TMAHC excited at 240 and 320 nm was also tested, as shown in Fig. 2(b) and 2(c). Under excitation at 240 nm, the emission peak at approximately 460 nm underwent thermal quenching as the temperature increased, and the luminescence center gradually shifted to 388 nm when the temperature was higher than 260 K, and the 388 nm emission showed anti-thermal quenching in the temperature range of 280–300 K. Under excitation of 320 nm, the emission peaks at 330 and 460 nm both showed thermal quenching.

It is worth noting that the 460 nm emission exhibits different temperature response characteristics under 240 nm excitation and 320 nm excitation. The bandgap energy can be utilized and explained for the anti-thermal quenching luminescence at low temperature of 460 nm emission excited by 240 nm and thermal quenching luminescence of 460 nm emission excited by 320 nm. The photon energy of 240 nm (5.17 eV) is higher than the band gap energy Eg of the TMAHC (4.80 V). This results in photogenerated free excitons, which are initially decoupled from the luminescence center. The dominant factors at this stage are carrier transport and capture efficiency at low temperatures, the carrier mobility is low and they are easily captured by shallow traps. At the same time, heating provides the thermal activation energy which lead electrons and holes escape from the shallow traps and more easily diffuse to the light-emitting center. Thus, it shows anti-thermal quenching at 80–200 K. The transport process has reached its optimal or saturated state as the temperature higher than 200 K, the thermal activation non-radiative quenching begins to exponentially increase and takes the dominant position, resulting in a decrease in the luminescence intensity. The photon energy of 320 nm (3.88 eV) is lower than the bandgap value, the photon energy is insufficient to excite electrons from the valence band to the conduction band, and it is completely impossible to generate free charge carriers. Since both excitation and emission occur within the same localized center, there is no carrier transport process. The only temperature-dependent process is the thermal quenching of the excited state of the emission center. Therefore, the intensity monotonically decreases with increasing temperature.

In order to investigate the two emission centers, the powder-dependent PL spectra were measured excited by a 265 nm light source, as shown in Fig. 2(e) and 2(f). In the PL spectrum, the integrated luminescence intensity of a single luminescent center is usually in accordance with the following power-law relationship with the excitation power: $I=k\times P^n$, where I represents the integrated intensity of the luminescence peak, k is a constant that is related to the concentration of the luminescent center, quantum efficiency, P is the excitation power, n is the exponent which value reveals the mechanism of luminescence. After Gaussian fitting peak separation and linear fitting, the scatter plots of log(I) versus log(P) for the are analyzed according to

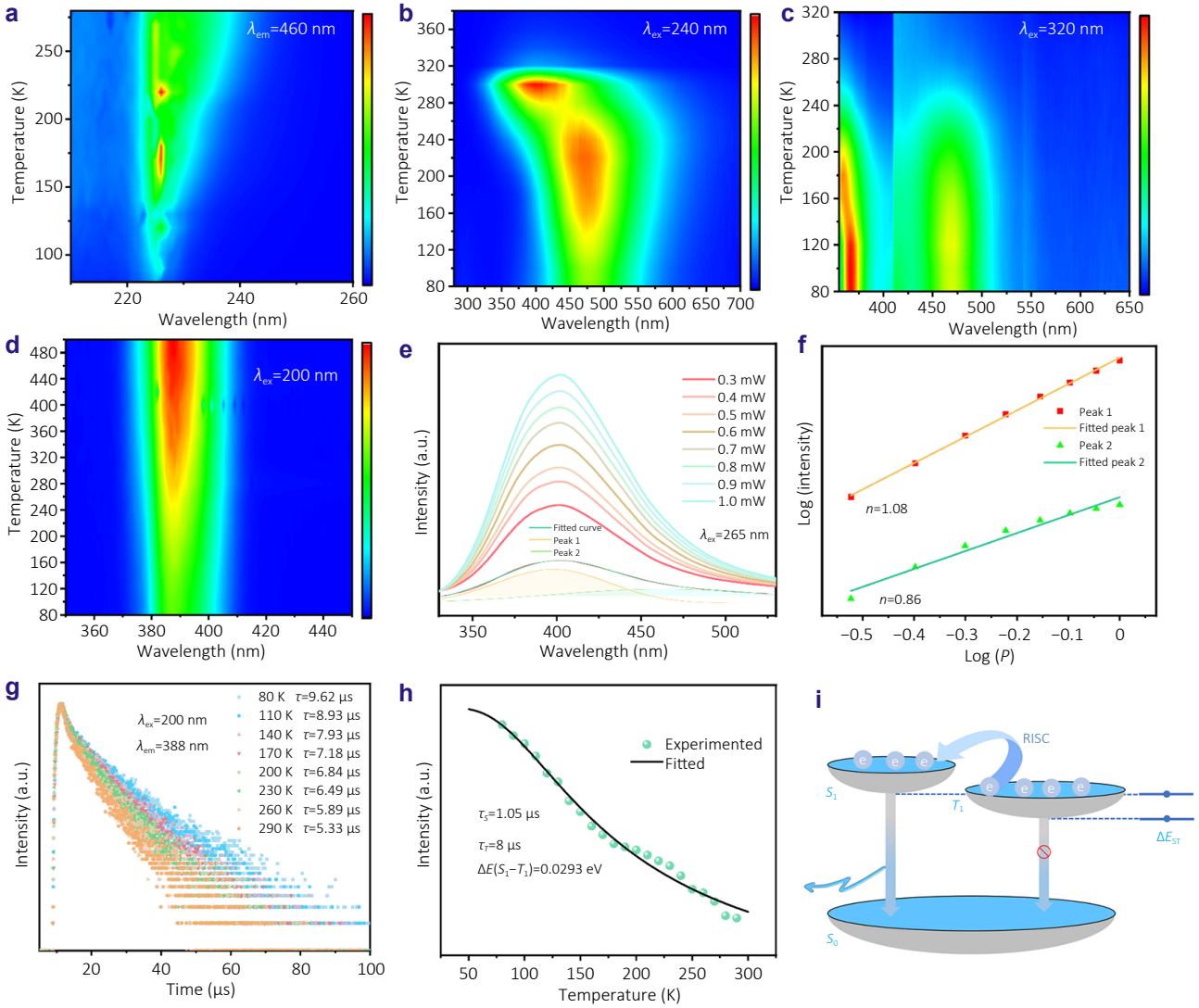

Fig. 2 | The temperature dependent PL performance of TMAHC. (a) The temperature dependent PLe spectra excited monitored at 460 nm. (b–d) The temperature dependent PL spectra excited at 240 nm, 320 nm, and 200 nm. (e) The excitation power-dependent PL spectra, the inset is Gaussian fitting peak separation. (f) The fitting of excitation power-dependent PL spectra. (g) Temperature dependent PL decay. (h) The fitting of temperature dependent PL decay. (i) The schematic diagram of reverse intersystem crossing.

$\log(I)=\log(k)+n\cdot\log(P)$. If $\log(I)$ has a linear relationship with $\log(P)$ in $y=a+bx$, the slope b is the power exponent n, and the intercept a is the $\log(k)$. Thus, for emission peak at 388 nm, n is 1.08, which corresponding to excitons related emission. For emission peak at 460 nm, n is 0.86, which originating from defects related emission. The calculated intensity of each luminescent center at P_0 is $I(P_0)=k\times P_0{}^n$. The proportion of total light emission accounted for by center A is $(I_A\ (P_0))/(I_A\ (P_0)+I_B\ (P_0))\times100\%$, while for center B is $(I_B\ (P_0))/(I_A\ (P_0)+I_B\ (P_0))\times100\%$. The proportion of 390 nm and 460 nm emission are calculated in Table S3. Which indicate as the power increases, the dominance of excitons related emission increases, while defect emission weakens relatively.

Further fitting of temperature dependent spectra can uncover the luminescence mechanism. Based on the relationship between the integrated fluorescence intensity and temperature, the Arrhenius formula was used to fit the thermal activation energy (E_b) of the excitons[34]:

$$I_T = \frac{I_0}{1+Ae^{-E_b/k_BT}}E_b\ , \tag{1}$$

where I_T and I_0 are the integrated PL intensities at temperatures of T K and 0 K, respectively, and A is the proportional coefficient. As shown in Fig. S8(a) and S8(c), the E_b values of TMAHC excited by 200 nm and 240 nm are 23.2 and 264.9 meV. The temperature-dependent PL of TTAHC and TPAHC excited at 200 nm was also tested, as shown in Fig. S9(a) and S9(d). Interestingly, TTAHC exhibited thermal quenching, whereas TPAHC exhibited anti-thermal quenching. As

shown in Fig. S9(b) and Fig. S9(e), the E_b values of TTAHC and TPAHC are 34.0 and 133.0 meV. Generally, the exciton binding energy is proportional to E_b; a larger exciton binding energy indicates high exciton stability and a low probability of exciton dissociation. In the context of TADF materials, a high exciton binding energy may impede the interconversion between singlet and triplet states, thereby inhibiting the manifestation of delayed fluorescence[35].

According to the relationship between the full width at half maximum (λ_{FWHM}) of the PL spectra and temperature, the Huang-Rhys factor was further fitted to measure the strength of the electron-phonon coupling[36]:

$$\lambda_{FWHM} = 2.36\sqrt{S}\hbar\omega_{phonon}\sqrt{\coth\left(\frac{\hbar\omega_{phonon}}{2k_BT}\right)}, \quad (2)$$

where the $\hbar\omega_{phonon}$ is phonon energy, the S is the Huang-Rhys factor. As shown in Fig. S8(c) and S8(d), the S parameters of TMAHC excited by 200 nm and 240 nm are 0.31 and 37.11, which indicate the strong lattice structure of 388 nm emission and soft lattice structure of 460 nm emission. Generally, as shown in Table S4, a soft lattice is a necessary condition for achieving efficient STE. As shown in Fig. S9(c) and Fig. S9(f), the S parameters of TTAHC and TPAHC excited by 200 nm are 0.38 and 1.74, respectively, indicating that the phonon coupling of TPAHC is much larger than that of the other two materials.

To verify the TADF mechanism of 388 nm emission of TMAHC, the temperature-dependent PL decay lifetimes were analyzed. As shown in Fig. 2(g), under 200 nm excitation, the PL decay lifetime of TMAHC increased as the temperature decreased. The temperature-dependent PL decay lifetime of TADF can be fitted using the following formula[37]:

$$\tau_{ave} = \frac{3 + \exp\left(-\frac{\Delta E(S_1 - T_1)}{k_BT}\right)}{3/\tau_T + 1/\tau_S * \exp\left(-\frac{\Delta E(S_1 - T_1)}{k_BT}\right)}, \quad (3)$$

where k_B is Boltzmann's constant, τ_S and τ_T are the fitted decay lifetimes of the S_1 and T_1 states, respectively, and $\Delta E(S_1{-}T_1)$ is the energy barrier between the S_1 and T_1 states. As shown in Fig. 2(h), the $\Delta E(S_1{-}T_1)$ value of TMAHC is 0.0293 eV. The PL decay lifetime of TTAHC and TPAHC under 200 nm excitation also investigated, as shown in Fig. S10(a)and Fig. S10(b). As shown in Fig. S10(c) and Fig. S10(d), the $\Delta E(S_1{-}T_1)$ values of TTAHC and TPAHC are 0.0417, 0.0917 eV, respectively. The $\Delta E(S_1{-}T_1)$ values of TTAHC and TMAHC are lower than that of Cs_2ZrCl_6 (0.069 eV)[38], indicating that TADF is easily realized in TMAHC and TTAHC through reverse intersystem crossing (RISC), whereas it is difficult in TPAHC. As shown of the schematic diagram of anti-intersystem crossing in Fig. 2(i), smaller $\Delta E(S_1{-}T_1)$ helps to more efficiently utilize triplet excitons, thus realized the TADF emission.

2.3 The scintillator characteratics

Previous works reported the excellent scintillation performance of TADF materials[39–41]. To explore the application prospects in X-ray detection and imaging, the scintillation performances of hafnium-based OIMHs were investigated. First, the X-ray absorption performances of CHC, hafnium-based OIMHs, commercial scintillators, and X-ray detectors were discussed based on the XCOM photon cross-section database[42]. As shown in Fig. 3(a), as the Cs^+ ions are substituted with organic cations, the X-ray absorption coefficients of the hafnium-based OIMHs become weaker than those of the commercial scintillators GAGG and LuAG. However, they are still stronger than those of silicon in the high energy range. The X-ray absorption coefficients of the hafnium-based OIMHs at 30–100 keV for X-ray imaging are displayed in Fig. S11(a), indicating a negative correlation between the absorption efficiency and carbon ion chain length. Figure S11(b) and S11(c) show the X-ray absorption efficiency of different scintillators under X-rays of 40 and 80 keV, respectively, which suggests that a scintillator screen with a sufficient thickness is required to effectively absorb X-rays. The X-ray-induced radiant luminescence (RL) of the hafnium-based OIMHs scintillators under X-ray irradiation with a dose rate of 878.93 $nGy_{air}{\cdot}s^{-1}$ is shown in Fig. 3(b), which indicates that the RL intensity can be regulated by the carbon chain length of the organic cations. The RL intensity increased with carbon chain length and peaked at TMAHC.

The light yield of bulk single-crystal scintillators is generally tested using pulse-height spectra, whereas the light yield values of powder or fragmentary single-crystal samples are underestimated owing to strong surface scattering. The widely used method for the light yield of metal halides is the reference method[39]; however, the light yield value is overestimated because of the strong scattering of the intense transverse light waveguide in the BGO standard sample and the neglect of the absorption of X-rays[15]. In this study, the light yield of Hf-based OIMHs was tested using the corrected reference method with full consideration of scintillator absorption. The complete test process is described in the experimental section. In short, by employing the CsI:Tl commercial scintillator screen, the gray value when the ray source was turned off was used as the background. When the X-ray source was turned on, the gray values of the placed and unplaced samples were recorded separately. After correction, the difference between the two is the X-ray absorption. Similarly, the prepared scintillator was placed in front of the CCD, and the gray value when the X-ray source was turned off was used as the background. The difference between the gray value when the X-ray source is turned on and the background can be similar to that of scintillator-light output. Considering spectral matching, the ratio of the number of emitted photons to the number of absorbed X-ray photons is the light yield. The X-ray imaging of scintillators captured by the CCD with an X-ray dose rate of

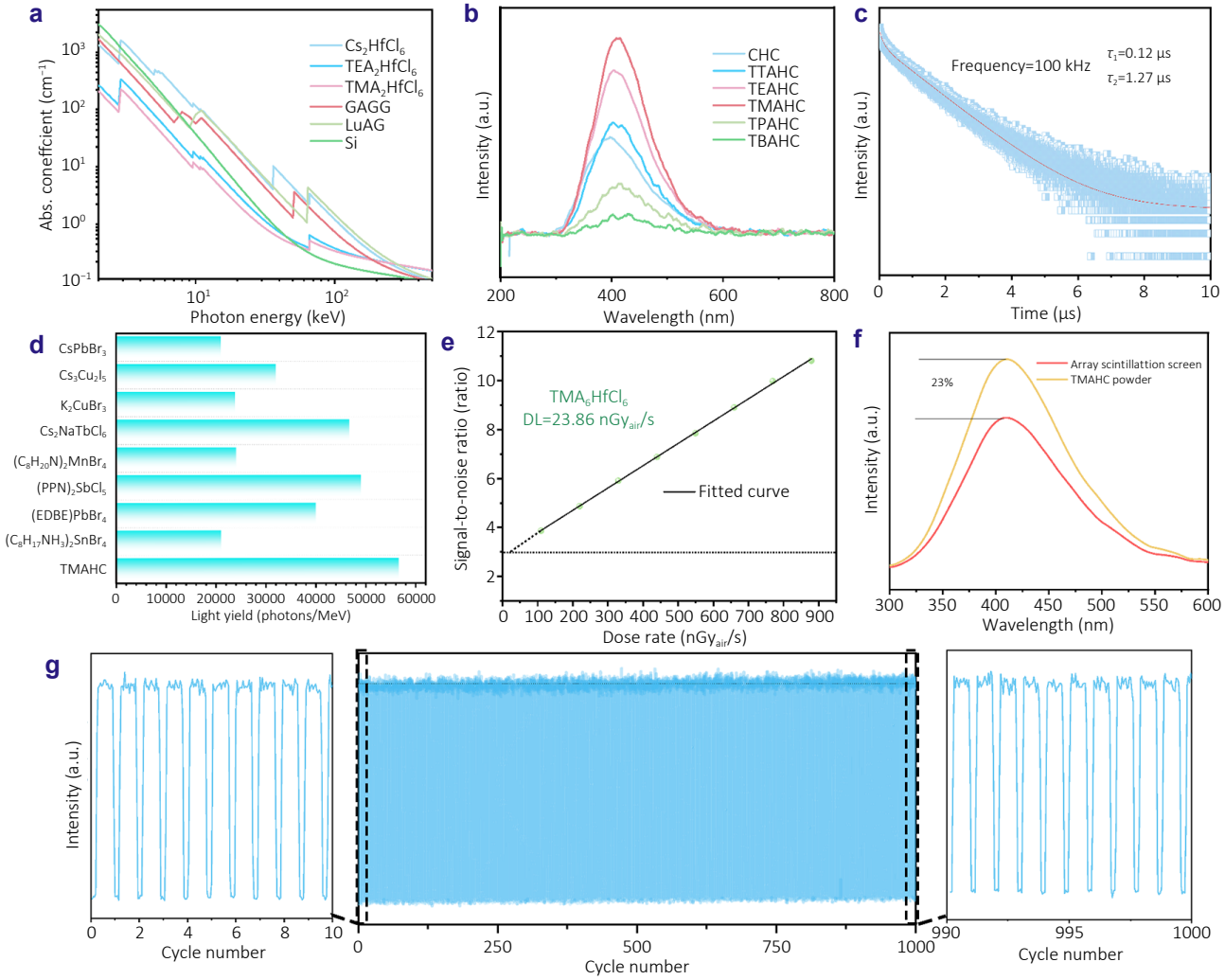

Fig. 3 | The X-ray scintillator characteristics of TMAHC. (a) The X-ray absorption coefficients of hafnium-based OIMHs. (b) The X-ray-induced RL of hafnium-based OIMHs. (c) The light yield comparison between TMAHC and other metal halides. (d) The RL spectra of TMAHC under various X-ray dose rates. (e) The detection limit of TMAHC. (f) The comparison of RL performance of TMAHC and scintillation screen. (g) The RL stability of TMAHC scintillation screen.

878.93 $nGy_{air}·s^{-1}$ is shown in Fig. S11(d). Evidently, TMAHC exhibits the strongest RL with a light yield of 56563±1250 photons/MeV. The RL spectra comparison of TMAHC and commercial scintillators are shown in Fig. S11(e), which verified the testing method and demonstrated the excellent performance of TMAHC. To investigate the RL mechanism, the RL decay life time was measured with excited light repetition frequency of 100 kHz. As shown in Fig. 3(c), which indicate that the fast component of 0.12 μs and slow component of 1.27 μs of RL, respectively correspond to TADF and STE. Figure 3(d) shows a comparison of the light yield of TMAHC with those of typical metal halide scintillators reported recently. $CsPbBr_3$ quantum dot (21000 photons/MeV)[43], $Cs_3Cu_2I_5$ crystal (32000 photons/MeV)[44], $Cs_2NaTbCl_6$ (52153 photons/MeV)[45] and typical manganese-based, antimony-based and tin-based OIMHs[16]. A complete comparison of the scintillator performance of hafnium-based OIMHs and other scintillators is listed in Table S5, which demonstrates the advantage of the RL performance of hafnium-based OIMHs.

In medical X-ray imaging, excessive dose rates cause radiation damage and side effects in patients. Therefore, the RL should be sufficiently high to maintain a strong signal. The RL intensities of TTAHC, TMAHC and TPAHC are presented in Fig. S11(f–h), where the RL intensity increases as the dose rate increases from 109.86 to 878.92 $nGy_{air}·s^{-1}$. The low detection limit is vital and can be calculated when the signal-to-noise ratio (SNR) is 3. As shown in Fig. 3(e), the detection limit of TMAHC is 23.86 $nGy_{air}·s^{-1}$, which is far below the minimum radiation dose required for medical applications (5.5 $μGy_{air}·s^{-1}$)[46]. As shown in Fig. S11(i), the detection limits proportional to the RL performance of scintillators. Radiation stability is related to the service performance of scintillators. The RL performance and stability of

the scintillation screen are crucial. Figure 3(f) shows that after packaging of the scintillation screen, the RL of TMAHC decreased by 23% due to changes of X-ray absorption efficiency and scattering. Figure 3(g) shows that the RL intensity is nearly constant under continuous X-ray irradiation at a dose rate of 878.92 $nGy_{air}·s^{-1}$, the RL intensity decreased by 3.2% after 1000 cycles, indicating the excellent radiation stability of TMAHC scintillation screen.

2.4 The luminescence mechanism

To explore the luminescence mechanism, a series of theoretical calculations of Hf-based OIMHs were carried out using density functional theory (DFT)[47], as expressed in the experiment section. Figure 4(a) shows the calculated bandgap of TMAHC is 4.36 eV. The density of states (DOS) in Fig. 4(b) indicate that Hf-5d orbitals constitute the conduction band minimum (CBM), whereas the Cl-3p orbit contributes to the valence band maximum (VBM). The large Hf-Hf distance reduces the interatomic orbital hybridization, resulting in a narrow Hf-5d of the CBM, which can achieve strong carrier localization by inducing local lattice polarization to trap electrons and stabilize the CBM[20]. The Cl-3p also shows narrow-band characteristics, which can localize charge carriers by forming small polarons and excitons. The calculated bandgaps of TTAHC and TPAHC are shown in Fig. S12(a) and S12(d), with value of 4.52 and 4.33 eV. The density of states (DOS) of the different elements in TTAHC

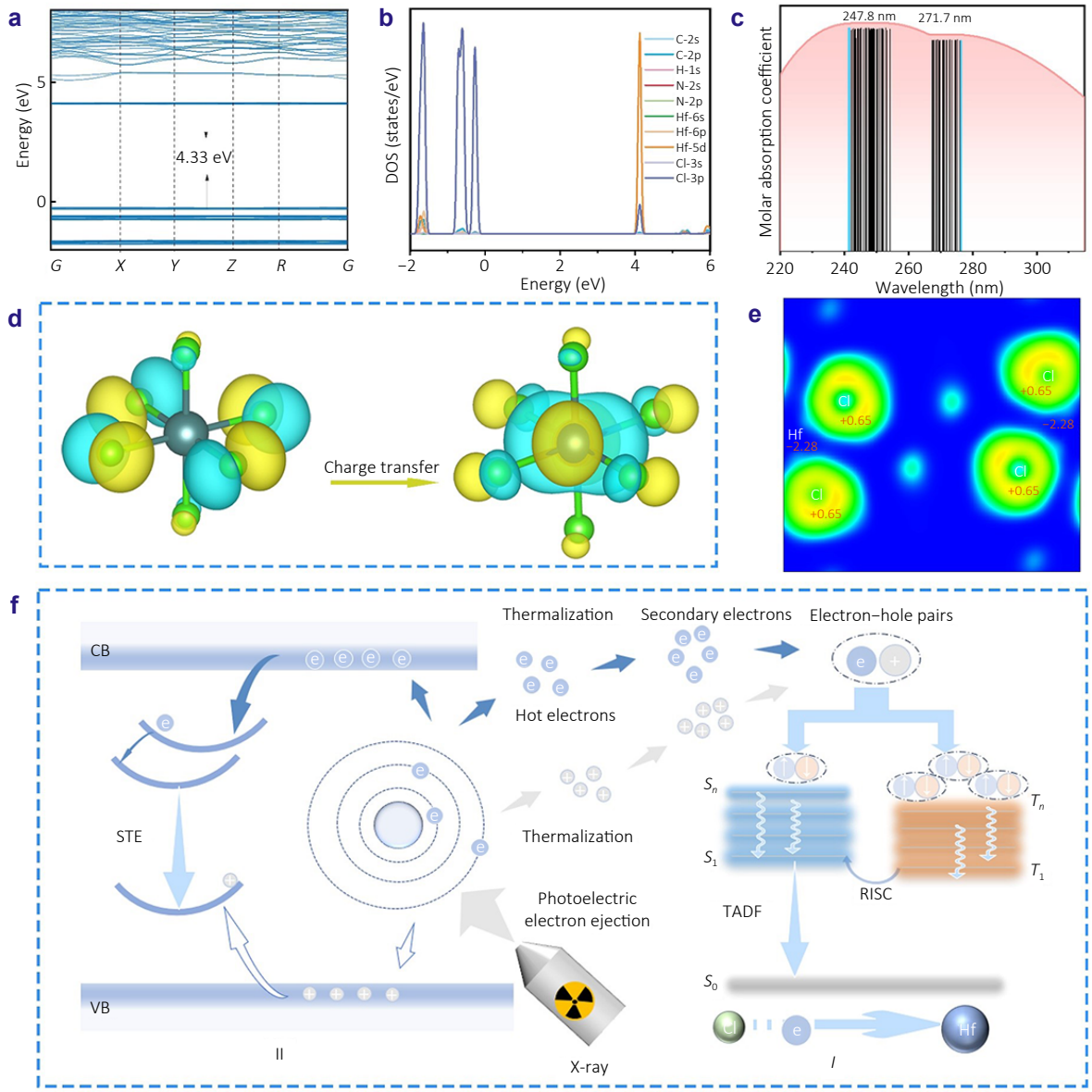

Fig. 4 | The DFT calculation of TMAHC. (a) The bandgap. (b) DOS. (c) The absorption spectrum calculated TD-DFT. (d) The HUMO and LUMO of TMAHC. (e) The ELF and Bader charge calculation. (f) The scheme of RL progress in TMAHC.

and TPAHC are displayed in Fig. S12(b) and S12(e), which indicate that the Hf-5d orbitals constitute the CBM and Cl-3p orbit constitute the VBM in TTAHC and TPAHC, respectively.

The PBE functional and DZVP-MOLOPT-SR-GTH basis set were employed for structural optimization and excited-state calculations. Based on the optimized ground-state structure, the singlet and triplet energy levels were calculated using time-dependent DFT (TD-DFT). To ensure complete absorption spectrum calculations, 100 excited states were computed (see Table S6). From the obtained absorption spectrum shown in Fig. 4(c), it can be seen that there is a strong absorption peak at 247 nm in this crystal, which corresponds to the excitation from S_0 to S_{67} energy level. The contributions of different orbital excitations were 32.4% for H-12 → L+4, 20.7% for H-9 → L+4, 9.8% for H-11 → L+3, and 6.6% for H-11 → L+5, respectively. The TD-DFT results indicated that the 247 nm absorption was due to the charge transfer from the highest occupied molecular orbital (HOMO) to the lowest unoccupied molecular orbital (LUMO). The HUMO and LUMO energies of TMAHC are displayed in Fig. 4(d), which are completely separated, indicating a strong charge-transfer trend. The electron localization function (ELF) and Bader charge calculations were employed for further analysis of the charge transfer in TMAHC, as shown in Fig. 4(e). The yellow Cl^- ions represent the loss of electrons, whereas the blue Hf^{4+} ions represent the gain of electrons. A large difference in the Bader charge indicates a high probability of charge transfer. The ELF and Bader charge calculations of TTAHC and TPAHC are shown in Fig. S11(c) and S11(f), which indicate a lower charge transfer than that of TMAHC. Thus, the light yield of Hf-based OIMHs is positively correlated with the intensity of charge transfer.

To further understand the charge transfer, the XPS binding energies of the Hf-based OIMHs were compared, as shown in Fig. S13. The electronic interaction between Cl and Hf is regulated by different organic cations. Owing to the different chemical environments of the Hf and Cl atoms, a change in the Hf-Cl chemical bond leads to a variation in the binding energy. Under X-ray irradiation, charge transfer occurs from Cl^+ ions to Hf^{4+} ions in hafnium-based metal halides. The electron cloud density around the Hf^{4+} ions increased, and the shielding effect on the inner electrons strengthened, thereby increasing the binding energy of the inner electrons of the Hf^{4+} ions. The temperature-dependent Raman spectra of TMAHC were measured to elucidate the temperature-dependent charge transfer, as shown in Fig. S14. The characteristic peaks at 165 cm^{-1} and 330 cm^{-1} originate from the T_{2g} and A_{1g} vibration modes of $[HfCl_6]^{2-}$[48]. As the temperature increased, the thermal expansion and anharmonicity effects caused a red-shift in the Raman modes. Simultaneously, the Raman spectral intensity increased with temperature, peaked at approximately 380 K, and then decreased. The possible reasons for this are the increase in thermally excited phonons, changes in the vibrational activity of the lattice or molecules, and enhancement of PL, which are consistent with temperature-related emission spectra. At high temperatures, the enhancement of lattice vibrations may lead to more active charge transfer.

The luminescence mechanism of TMAHC can be deduced from a series of spectroscopic and theoretical calculations. Four different emission bands were observed in the PL spectra. The 388 nm emission originated from TADF associated with charge transfer states owing to inverse temperature quenching emission and regulation of the temperature-dependent PL decay lifetime. The 330 nm peak originated from an intrinsic transition due to band gap matching. The 460 and 570 nm emissions originated from STE due to the broadband emission and temperature-dependent PL behavior, which is similar to the previously reported quantum chemical calculation results regarding the STEs emission of CHC[20]. TADF emission can be employed to explain the ultrahigh RL of Hf-based OIMHs and the mediocre PL. The scheme of RL progress in TMAHC is shown in Fig. 4(f). When X-rays strike the scintillator, they cause the atoms within it to undergo photoionization. Simultaneously, the *K*-shell electrons of the atoms absorb the energy of the X-rays and break free from the atomic nucleus, becoming photoelectrons. Subsequently, the outer-shell electrons transition to the *K*-shell to fill the vacancy, and the excess energy is dissipated through two pathways. One part transfers the energy to other electrons, making them Auger electrons, and the other part is released as characteristic X-rays. These characteristic X-rays participate in the above process to generate secondary electrons. The high-energy electrons generated during X-ray absorption are ionized through collisions, continuously generating secondary electrons and characteristic X-rays. A large number of holes are left in the core or valence band, initiating the electron-multiplication process. At this time, the high-energy electrons and holes relax to the conduction band bottom and valence band top through thermal activation, respectively. Electrons and holes are confined on $[HfCl_6]^{2-}$, bound together by Coulomb force, forming excitons. Some of the thermally activated electrons form charge transfer from Cl to Hf in TADF, while the other free excitons are further bound to form STE, and radiative recombination emits visible photons. Yang et al. confirmed that under radiation stimulation, the ratio of singlet to triplet excitons is 1:3[39]. If triplet excitons that do not contribute to luminescence are converted into emissive singlet excitons, a higher light yield can be achieved.

During the generation and transport of excitons in the RL, defects in the scintillator material capture excitons, resulting in a decrease in the light output. To investigate the influence of defects on the performance of radiation detection, considering that the most likely defect to form in the hafnium-based metal halide is the Cl vacancy[20], the formation energies of the Cl vacancies in CHC and TMAHC were

calculated using DFT. Supercells of CHC and TMAHC were then constructed. The calculated Cl-vacancy formation energy in CHC is 4.18 eV, whereas that in TMAHC is 4.43 eV. A higher vacancy formation energy indicates that Cl vacancies are more difficult to form in TMAHC than in CHC. To verify this conclusion, 3D thermoluminescence (TL) spectra of CHC and TMAHC were obtained. The sample was exposed to X-rays for 10 min, with a temperature increase rate of 5 °C/s and a temperature ranging from 80 to 600 K. As shown in Fig. S15(a). CHC showed a strong signal with an emission consistent with RL and two TL peaks at 150 K and 250 K. The defect energy levels of CHC at depths of 0.5 eV and 0.6 eV can be calculated using the equation $E_{\mathrm{Trap}}= T_m(\mathrm{K})/500(\mathrm{K})\ (T_m)$[49]. As shown in Fig. S15(b), there is no TL signal observed in TMAHC, indicating its low defect density. This suggests that fewer electrons are captured by the defects in TMAHC, resulting in a higher light output than that of CHC.

2.5 The X-ray imaging performace

Owing to its high light yield, TMAHC is expected to be used in X-ray imaging. Guiding light propagation toward its corresponding pixel detector is the key point for high-quality X-ray imaging[8]. Pixelated scintillation screens can restrain the lateral spreading of scintillation light and improve X-ray absorption for better signal-to-noise ratio, thus improving the spatial resolution of X-ray imaging[50]. However, traditional melt processing methods for pixelated scintillation screen fabrication are expensive and complex[51], and scintillation screens structured by anodic aluminum oxide are easy to deform, leading to an unsatisfactory spatial resolution of 10.4 lp/mm[52]. Yang et al. reported the Hf-based OIMHs can be developed into luminous inks for 3D printing of specific shapes[53], which provided a paradigm for more convenient array processing.

To verify the suppression effect of the array scintillator screen on optical crosstalk, Zemax Optic Studio was used to simulate the fluorescence crosstalk of the scintillation screen, aiming to explain processes such as the reflection and refraction of the light beam. The main parameters of the simulation are listed in Table S7, and are consistent with the experimental conditions. The luminous ink was composed of fluororubber, TMAHC, and acetone, and array apertures of 5, 12.5, and 25 μm with a depth of 100 μm were considered. The simulation results are presented in Fig. S16, by employing non-sequential ray tracing, 50 rays of light emitted from the top layer of the scintillator inside the array were tracked. Figure S16 (a) and Fig. S16(b) show the optical path simulation within the scintillator array with a 5 μm aperture. Figure S16 (c) shows the fluorescence distribution in the central pixel of a single particle on the surface layer of the particle. Similarly, Fig. S16(d)–(i) show the above parameters of the scintillator array with 12.5 and 25 μm apertures, respectively. Figure S17(a) shows the column cross-section of Fig. S16 (c, f), and S16(i), which indicate that as the aperture of the array scintillation screen increases, the optical crosstalk rate is approximately 2%, 4%, and 5%, respectively. Figure S17(b) shows the geometric modulation transfer function obtained by performing the Fourier transform on Fig. S16(a) and normalizing them. As the array aperture increases, the spatial resolution is successively 31.82 lp/mm, 63.15 lp/mm, and 95.01 lp/mm when the modulation degree is 0.2. The optical crosstalk simulation indicated that as the pixel array structure was constructed, the light output in the vertical direction increased and the light crosstalk decreased. Moreover, the smaller the array aperture lead lower the light crosstalk.

Silicon wafers with a diameter of 4 inch (1 inch=2.54 cm) and a thickness of 200 μm were used in this work. A series of array structures with a hole depth of 100 μm and hole diameters of 5, 12.5, 25, 50, and 100 μm were processed, as shown in Fig. S18(a). The scheme of the array scintillator screen fabrication progress is shown in Fig. 5(a). First, the TMAHC was dispersed in an acetone solution of fluororubber and processed into luminous ink. The silicon templates were then immersed in luminous ink and filled while maintaining a high vacuum. The array scintillation screens exhibited a slight white color under daylight and bright blue emission under 254 nm light. A SEM was used to examine the filling of the scintillator screen.

Figure S18(b–f) show the top view of the TMAHC array scintillation screens with apertures of 5, 12.5, 25, 50, and 100 μm, indicating that a larger aperture size leads to a higher filling degree of the scintillator material, with filling rate of 5%, 50%, 95%, 100% and 100% respectively. The array scintillation screens with apertures larger than 25 μm were fully populated, whereas scintillators rarely existed within the array scintillation screens with apertures of 5 and 12.5 μm. The morphology of the array scintillation screens with a 25 μm aperture was further investigated, as shown in Fig. 5(b–d). Figure 5(b) shows the top view in a large field of view, and Fig. 5(c) and 5(d) show the cross-sections of the silicon array tested using SEM and an optical microscope, respectively. This indicates an even distribution of TMAHC in the array scintillation screen, and such a simple solution-based method for preparing array scintillation screens is conducive to large-scale production. X-ray imaging of the array scintillation screens was performed using an imaging system with lens coupling. After passing through the sample to be tested and the scintillation screen, the X-rays are converted into light signals. The light signals were then reflected by a reflector to the camera for imaging. The photons in the array scintillation screen can only propagate within the array channels, thereby reducing lateral light crosstalk. The spatial resolution of the TMAHC array scintillation screens was measured using the ISO 19232 duplex-wire image quality indicator as shown in Fig. S19[54], and the relationship between the duplex wire numbers and spatial resolution is listed in Table S8.

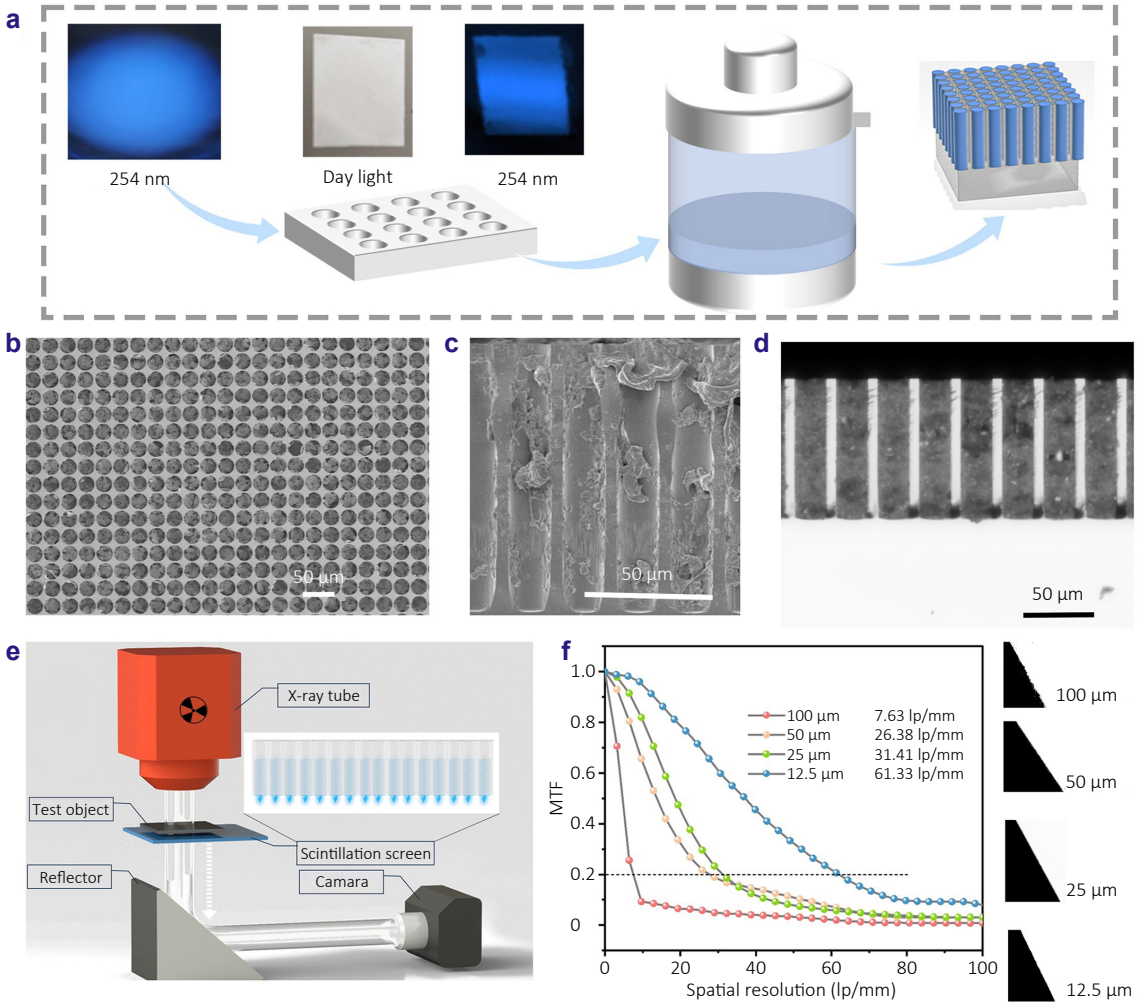

Fig. 5 | The TMAHC array scintillator screen. (a) Scheme of fabrication progress. (b, c) The top view and cross-section of silicon array tested by SEM with aperture of 25 μm. (d) The cross-section of silicon array tested by optical microscope with aperture of 25 μm. (e) Scheme of X-ray imaging system. (f) The MTF testing using the knife edge method.

As shown in Fig. S20, spatial resolution of different specifications of array scintillation screens measured by duplex-wire image quality indicator. Figure S20(a–c) show the X-ray imaging of the duplex-wire image quality indicator using array scintillation screens with apertures of 12.5, 25, and 50 μm. The corresponding grayscale images are presented in Fig. S20(d–f) are the corresponding grayscale. This indicates that all the array scintillation screens achieved a high spatial resolution above 25 lp/mm. The modulation transfer function (MTF) was employed to further investigate the spatial resolution of the different array scintillation screens. The knife-edge method is one of the main approaches for measuring the MTF of X-ray detectors[55], which obtains the MTF by calculating the line spread function (LSF) of the system. The MTF of the array scintillation screens with apertures of 12.5, 25, 50, and 100 μm are shown in Fig. 5(f). When the MTF is 0.2, the corresponding spatial resolutions are 66.33, 31.41, 26.38, and 7.63 lp/mm, which are slightly lower than the simulation results, due to the existence of optical crosstalk in the channels. It can be expected that the spatial resolution of our array scintillator screen still has a large room for improvement by further optimizing the filling degree and transparency inside the arrays. Our fabricated array scintillation screens exhibited a higher spatial resolution than commercial scintillation screens such as GOS[10] and CsI:Tl[11]. Table S9 lists the TMAHC array scintillation screen performance comparisons of the TMAHC array screens and reported metal halide scintillation screens, indicating its superior spatial resolution.

To validate the X-ray imaging performance of the TMAHC array scintillation screen, chips representing industrial applications and nude mice representing biomedical applications were used as test objects. The scintillator screen with an aperture size of 12.5 μm shows a high spatial resolution, but its insufficient filling causes low X-ray absorption and light output. Therefore, a scintillator screen with an

aperture size of 25 μm was selected for X-ray imaging. Figure 6(b) shows the X-ray imaging of a chip displayed in Fig. 6(a). The hollow structure inside the chip and the bonded gold wire with a diameter of 20 μm can be clearly observed, with sharp image edges. Figure 6(c) shows the local enlarged drawing of the imaging in Fig. 6(b), and the solder joint between the gold wire and chip can be observed clearly. It is worth noting that the metal halide scintillator screen cannot achieve the ability to image the internal leads of the chip; only the pins can be observed[56–62]. Moreover, the chip in Fig. 6(a) was also imaged by commercial medicine scintillation screen in RAD SPEED M system (SHZMADZU), as shown in Fig. 6(d). The outline of the chip pins can be recognized, but the details cannot be recognized, which indicate the leading-edge spatial resolution of TMAHC array scintillation screen. To further verify the application of the TMAHC array scintillation screen in biomedicine, as shown in Fig. 6(e), a BALB/c-nu athymic nude mouse was selected for X-ray imaging. As can be clearly observed in Fig. 6(f), the fracture condition of the mouse leg bone can be distinguished, and the bone spurs after the fracture can be identified, which plays an auxiliary role in precise medical diagnosis and treatment. Figure 6(g) indicates that the ear cartilage tissue and tiny front paw bones of the mouse can be distinguished. The TMAHC array scintillation screen has high-quality X-ray imaging. Based on the imaging effects of the chip and biological samples, the TMAHC array scintillation screen has promising application prospects in industry and biomedicine.

3 Conclusions

In this study, we designed and synthesized a series of Hf-based organic-inorganic metal halides. The quality of X-ray imaging is restricted by the excitation's regulation of light management. The thermally activated delayed fluorescence was demonstrated by a series of PL characteristics and theoretical calculations. The non-luminescent triplet excitons became emissive, improving the utilization rate of excitons and increasing the light output of scintillators up to 56563.31 photons/MeV and detection limit of 23.86 nGy_{air}/s. Moreover, the optical crosstalk was suppressed by developing silicon array scintillation screens, resulting in a spatial resolution of up to 31.41 lp/mm. It is worth noting that the

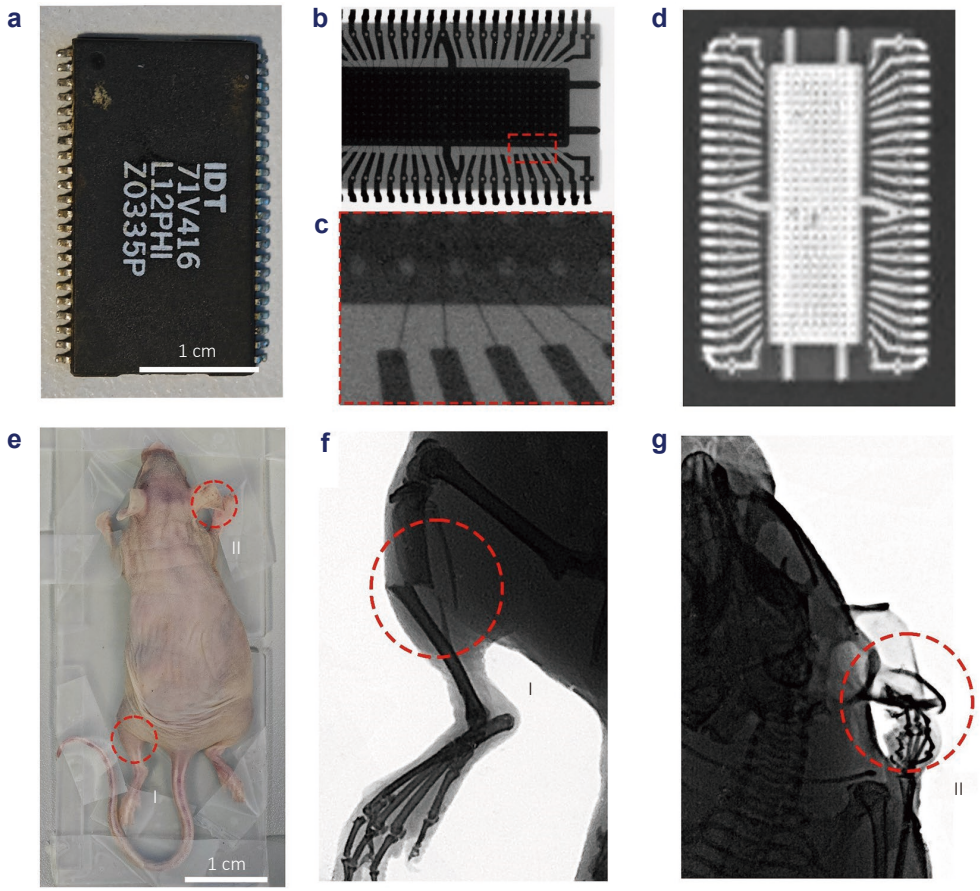

Fig. 6 | The X-ray imaging of TMAHC array scintillation screens with aperture of 25 μm. (a) The photo of a chip. (b) The X-ray imaging of chip by TMAHC array scintillation screen. (c) The detail of X-ray imaging in (b). (d) The X-ray imaging of chip by commercial medicine scintillation screen. (e) The photo of a nude mouse. (f) and (g) The X-ray imaging of nude mouse by TMAHC array scintillation.

X-ray imaging performance of the Hf-based metal halide scintillation screens in this study still has significant room for improvement. In summary, this study provides a convenient and high-performance scintillator screen fabrication strategy for X-ray imaging in industrial and medical applications.

4 Experimental section

The details of experimental methods can be found in the Supplementary information.

References

1. Wu HD, Ge YS, Niu GD et al. Metal halide perovskites for X-ray detection and imaging. *Matter* **4**, 144–163 (2021).
2. Jana A, Cho S, Patil SA et al. Perovskite: scintillators, direct detectors, and X-ray imagers. *Mater Today* **55**, 110–136 (2022).
3. Han MY, Xiao YR, Zhou C et al. Recent advances on two-dimensional metal halide perovskite x-ray detectors. *Mater Futur* **2**, 012104 (2023).
4. Ou XY, Chen X, Xu XN et al. Recent development in X-ray imaging technology: future and challenges. *Research* **2021**, 9892152 (2021).
5. Withers PJ, Bouman C, Carmignato S et al. X-ray computed tomography. *Nat Rev Methods Primers* **1**, 18 (2021).
6. Liu RK, Li F, Zeng F et al. Halide perovskite x-ray detectors: fundamentals, progress, and outlook. *Appl Phys Rev* **11**, 021327 (2024).
7. Wang YM, Li M, Chai ZF et al. Perovskite scintillators for improved X-ray detection and imaging. *Angew Chem Int Ed* **62**, e202304638 (2023).
8. Xu XW, Xie YM, Shi H et al. Light management of metal halide scintillators for high-resolution X-ray imaging. *Adv Mater* **36**, 2303738 (2024).
9. Cha BK, Shin JY, Kim JY et al. Fabrication and comparison Gd2O2S(Tb) and CsI(TL) films for X-ray imaging detector application. In *Proceedings of 2008 IEEE Nuclear Science Symposium Conference Record* 1232–1235 (IEEE, 2008). http://doi.org/10.1109/NSSMIC.2008.4774627.
10. Heo JH, Shin DH, Park JK et al. High-performance next-generation perovskite nanocrystal scintillator for nondestructive X-ray imaging. *Adv Mater* **30**, 1801743 (2018).
11. Zhao BZ, Qin XB, Feng ZD et al. Performance evaluation of CsI screens for X-ray imaging. *Chin Phys C* **38**, 116003 (2014).
12. Weber MJ. Inorganic scintillators: today and tomorrow. *J Lumin* **100**, 35–45 (2002).
13. Zhou Q, Li W, Xiao JW et al. Low-dimensional metal halide for high performance scintillators. *Adv Funct Mater* **34**, 2402902 (2024).
14. Chen QS, Wu J, Ou X et al. All-inorganic perovskite nanocrystal scintillators. *Nature* **561**, 88–93 (2018).
15. Li XM, Hu XD, Li CK et al. Are inorganic lead halide perovskite nanocrystals promising scintillators. *ACS Energy Lett* **8**, 2996–3004 (2023).
16. Zhou C, Han MY, Xiao YR et al. Lead-free perovskites and derivatives enable direct and scintillation-type X-ray detection. *Mater Sci Eng R Rep* **156**, 100756 (2023).
17. Burger A, Rowe E, Groza M et al. Cesium hafnium chloride: a high light yield, non-hygroscopic cubic crystal scintillator for gamma spectroscopy. *Appl Phys Lett* **107**, 143505 (2015).
18. Nagorny S. Novel Cs_2HfCl_6 crystal scintillator: recent progress and perspectives. *Physics* **3**, 320–351 (2021).
19. Liu SP, Yang B, Chen JS et al. Colloidal synthesis and tunable multicolor emission of vacancy-ordered Cs_2HfCl_6 perovskite nanocrystals. *Laser Photon Rev* **16**, 2100439 (2022).
20. Kang B, Biswas K. Carrier self-trapping and luminescence in intrinsically activated scintillator: cesium hafnium chloride (Cs_2HfCl_6). *J Phys Chem C* **120**, 12187–12195 (2016).
21. Král R, Babin V, Mihóková E et al. Luminescence and charge trapping in Cs_2HfCl_6 single crystals: optical and magnetic resonance spectroscopy study. *J Phys Chem C* **121**, 12375–12382 (2017).
22. Buryi M, Babin V, Ligthart RAM et al. Correlation of emission, scintillation and charge trapping properties in Cs_2HfCl_6 and Cs_2ZrCl_6 single crystals. *J Mater Chem C* **9**, 2955–2968 (2021).
23. Saeki K, Fujimoto Y, Koshimizu M et al. Comparative study of scintillation properties of Cs_2HfCl_6 and Cs_2ZrCl_6. *Appl Phys Express* **9**, 042602 (2016).
24. Maughan AE, Ganose AM, Scanlon DO et al. Perspectives and design principles of vacancy-ordered double perovskite halide semiconductors. *Chem Mater* **31**, 1184–1195 (2019).
25. Morgan EE, Kent GT, Zohar A et al. Hybrid and inorganic vacancy-ordered double perovskites A_2WCl_6. *Chem Mater* **35**, 7032–7038 (2023).
26. Liu SP, Yang B, Chen JS et al. Efficient thermally activated delayed fluorescence from all-inorganic cesium zirconium halide perovskite nanocrystals. *Angew Chem Int Ed* **59**, 21925–21929 (2020).
27. Li TY, Zheng SJ, Djurovich PI et al. Two-coordinate thermally activated delayed fluorescence coinage metal complexes: molecular design, photophysical characters, and device application. *Chem Rev* **124**, 4332–4392 (2024).
28. Lin ZG, Zhu SQ, Wang Z et al. Ultra-fast on-chip VUV (λ<200 nm) photodiode integration. *Mater Today* **86**, 202–209 (2025).
29. Zhu SQ, Lin ZG, Wang Z et al. Vacuum-ultraviolet (λ < 200 nm) photodetector array. *PhotoniX* **5**, 5 (2024).
30. Hao XR, Liu HL, Ding WG et al. Zn^{2+}-doped lead-free $CsMnCl_3$ nanocrystals enable efficient red emission with a high photoluminescence quantum yield. *J Phys Chem Lett* **13**, 4688–4694 (2022).
31. Nobbs JH. Kubelka-Munk theory and the prediction of reflectance. *Rev Prog Color Relat Top* **15**, 66–75 (1985).
32. Saeki K, Wakai Y, Fujimoto Y et al. Luminescence and scintillation properties of Rb_2HfCl_6 crystals. *Jpn J Appl Phys* **55**, 110311 (2016).
33. Feng JY, Wang ZY, Xu HY et al. The charge transfer band as a key to study the site selection preference of Eu^{3+} in inorganic crystals. *Inorg Chem* **60**, 19440–19447 (2021).
34. Chen Z, Yu CL, Shum K et al. Photoluminescence study of polycrystalline $CsSnI_3$ thin films: determination of exciton binding energy. *J Lumin* **132**, 345–349 (2012).
35. Lan ZA, Zhang GG, Chen X et al. Reducing the Exciton binding energy of donor–acceptor-based conjugated polymers to promote charge-induced reactions. *Angew Chem Int Ed* **58**, 10236–10240 (2019).
36. Ryu JH, Won HS, Park YG et al. Synthesis of $Eu_xSi_{6-z}Al_zO_zN_{8-z}$ green phosphor and its luminescent properties. *Appl Phys A* **95**, 747–752 (2009).
37. Azumi T, O'Donnell CM, McGlynn SP. On the multiplicity of the phosphorescent state of organic molecules. *J Chem Phys* **45**, 2735–2742 (1966).
38. Zhang F, Zhou YC, Chen ZP et al. Thermally activated delayed fluorescence zirconium - based perovskites for large - area and ultra-flexible X - ray scintillator screens. *Adv Mater* **34**, 2204801 (2022).
39. Ma WB, Su YR, Zhang QS et al. Thermally activated delayed fluorescence (TADF) organic molecules for efficient X-ray scintillation and imaging. *Nat Mater* **21**, 210–216 (2021).
40. Wang JX, Dutta I, Yin J et al. Triplet-triplet energy-transfer-based transparent X-ray imaging scintillators. *Matter* **6**, 217–225 (2023).
41. He J, He L, Zhang MY et al. Heterocluster-assembled crystalline hydrophobic complexes with delayed fluorescence. *Adv Mater* **37**, 2505734 (2025).

42. Berger MJ, Hubbell JH. *XCOM: Photon cross sections on a personal computer*. National Bureau of Standards, Washington, DC (USA). Center for Radiation Research. https://www.nist.gov/pml/xcom-photon-cross-sections-database.
43. Zhang YH, Sun RJ, Ou XY et al. Metal halide perovskite nanosheet for X-ray high-resolution scintillation imaging screens. *ACS Nano* **13**, 2520–2525 (2019).
44. Cheng SL, Beitlerova A, Kucerkova R et al. Zero-dimensional $Cs_3Cu_2I_5$ perovskite single crystal as sensitive X-ray and γ-ray scintillator. *Phys Status Solidi Rapid Res Lett* **14**, 2000374 (2020).
45. Wang ZL, Xu XM, Wang SH et al. Cerium doping double perovskite scintillator for sensitive X-ray detection and imaging. *Chem Eur J* **27**, 9071–9076 (2021).
46. Devanathan R, Corrales LR, Gao F et al. Signal variance in gamma-ray detectors-a review. *Nucl Instrum Methods Phys Res Sect A Accel Spectrom Dect Assoc Equip* **565**, 637–649 (2006).
47. Kresse G, Furthmüller J. Efficient iterative schemes for *ab initio* total-energy calculations using a plane-wave basis set. *Phys Rev B* **54**, 11169–11186 (1996).
48. Jiang JL, Zheng JJ, Fu H et al. Scalable and room-temperature preparation of Cs_2HfCl_6 double perovskites with recorded photoluminescence efficiency and robust stability. *Chem Eng J* **479**, 147543 (2024).
49. Li ZJ, Yu N, Zhou JJ et al. Coloring afterglow nanoparticles for high-contrast time-gating-free multiplex luminescence imaging. *Adv Mater* **32**, 2003881 (2020).
50. Liu S, Gu M, Chen H et al. Performance of pixelated CsI scintillation screen with hexagonal array arrangement prepared by vacuum melting injection method. *Nucl Instrum Methods Phys Res Sect A Accel Spectrom Dect Assoc Equip* **903**, 18–24 (2018).
51. Teng YX, Gu M, Sun ZX et al. Structured $Cs_3Cu_2I_5$ scintillation screen based on oxidized silicon micropore array template for high-resolution X-ray imaging. *J Lumin* **263**, 120116 (2023).
52. Zhao X, Jin T, Gao WR et al. Embedding $Cs_3Cu_2I_5$ scintillators into anodic aluminum oxide matrix for high-resolution X-ray imaging. *Adv Opt Mater* **9**, 2101194 (2021).
53. Zhu C, Jin JB, Wang Z et al. Supramolecular assembly of blue and green halide perovskites with near-unity photoluminescence. *Science* **383**, 86–93 (2024).
54. International Organization for Standardization. Non-destructive testing — Image quality of radiographs — part 5: Determination of the image unsharpness value using duplex wire-type image quality indicators, ISO 19232–5: 2013(E). International Organization for Standardization. https://standards.iteh.ai/catalog/standards/sist/84b10043-27df-49fd-a8cc-8cd31583d589/iso-19232-5-2013
55. Samei E, Flynn MJ, Reimann DA. A method for measuring the pre-sampled MTF of digital radiographic systems using an edge test device. *Med Phys* **25**, 102–113 (1998).
56. Zhou JE, An K, He P et al. Solution-processed lead-free perovskite nanocrystal scintillators for high-resolution X-ray CT imaging. *Adv Opt Mater* **9**, 2002144 (2021).
57. Yang LW, Li ZY, He LW et al. Emergence of a lanthanide chalcogenide as an ideal scintillator for a flexible X-ray detector. *Angew Chem Int Ed* **62**, e202306465 (2023).
58. Hu QS, Zhang CK, Wu X et al. Highly effective hybrid copper(I) iodide cluster emitter with negative thermal quenched phosphorescence for X-ray imaging. *Angew Chem Int Ed* **62**, e202217784 (2023).
59. Chen TH, Xu YL, Ying A et al. Through‐space charge‐transfer organogold(III) complexes enable high‐performance X‐ray scintillation and imaging. *Angew Chem* **136**, e202401833 (2024).
60. Yang ZJ, Zhang P, Chen XF et al. High-confidentiality X-ray imaging encryption using prolonged imperceptible radioluminescence memory scintillators. *Adv Mater* **35**, 2309413 (2023).
61. Chen JH, Luo JB, Peng QP et al. Branched alkyl chains tunable organic-inorganic hybrid manganese halides for anti-counterfeiting, white light-emitting diode and X-ray imaging applications. *Angew Chem Int Ed* **64**, e202508536 (2025).
62. Zhang W, Sui P, Zheng W et al. Pseudo-2D layered organic-inorganic manganese bromide with a near-unity photoluminescence quantum yield for white light-emitting diode and X-ray scintillator. *Angew Chem Int Ed* **62**, e202309230 (2023).

Acknowledgements

This work acquired financial support from National Natural Science Foundation of China (62375032, 61975023); Natural Science Foundation of Chongqing (No. CSTB2023TIAD-KPX0017, CSTB2022NSCQ-MSX0360); The Open Fund of the State Key Laboratory of High Field Laser Physics (Shanghai Institute of Optics and Fine Mechanics).

Competing interests

The authors declare no competing financial interests.

Supplementary information

Supplementary information for this paper is available at https://doi.org/10.29026/oea.2026.250273